CHAPTER IV
SYNTHESIS AND ACTIVITY OF Ti-Fe-SBA-15 FROM SILATRANE

4.1 Abstract

Monomeric- and bimetallic-incorporated SBA-15 (Fe-SBA-15, Ti-SBA-15 and 0.01Fe-0.01Ti-SBA-15) were successfully synthesized via sol gel process at room temperature in highly acidic condition using silatrane, ferric chloride and titanium isopropoxide as a silica, iron, and titanium sources, respectively, Pluronic 123 as template. It was found that from SAXS patterns and FE-SEM images all samples maintained their 2D hexagonal mesoporous structure. The result from N_2 adsorption-desorption measurement showed type (IV) isotherm with H1 hysteresis loop and uniform pores as well as high surface area (631–763 m^2/g), pore volume (0.621-0.971 cc/g), and large pore size (3.93–5.21 nm). DR-UV spectra confirmed the metal incorporation with no extraframework. Its catalytic activity was studied for phenol hydroxylation using H_2O_2 as oxidizing agent and showed that the highest phenol conversion at 37.96% with 100% selectivity of benzoquinone was obtained when using 1:1 molar ratio of phenol/H_2O_2 and 30 mg of 0.01Fe-0.01Ti-SBA-15 at 30 °C for 20 min. Metal leaching is not observed. However, the catalyst cannot be reused due to its instability.

(**Keywords**: SBA-15, Silatrane, Iron, Titanium, Phenol hydroxylation)

4.2 Introduction

SBA-15 (Santa Barbara Amorphous) has hexagonally ordered cylindrical pores synthesized using P123 (triblock copolymer of $PEO_{20}PPO_{70}PEO_{20}$) as surfactant, and used in many applications namely, support for catalyst, separation [1-4] since it possesses various advantages such as high specific surface area, larger pore size and thicker wall compared to MCM-41, which improve hydrothermal stability [5, 6].

Generally, SBA-15 is synthesized in highly acidic condition, using tetraethylorthosilicate (TEOS) as silica source and P123 as structure-directing agent [3, 7]. However, TEOS is expensive precursor, moisture sensitive, and need hydrothermal condition to synthesize. Wongkasemjit and coworkers synthesized SBA-15 at room temperature using silatrane as a silica source due to moisture stability of the silatrane [4]. Pure SBA-15 itself lacks of some redox properties, thus many scholars tried to incorporate some heteroatoms or transition metals to improve the properties [6, 8]. Many researchers successfully added some multicomponents into SBA-15 framework [6, 8]. Some researchers also found that Fe and Ti show some superb properties in various reactions [9-11].

As well-known, phenol was harmful for living things [12]. A way to decrease its toxicity is to turn phenol into the other less toxic forms. For example, phenol hydroxylation is a reaction to convert phenol to mild products, such as catechol (CAT), hydroquinone (HQ), and benzoquinone (BQ), being used in various applications [13, 14].

The aims of this work are thus to synthesize bimetallic iron/titanium SBA-15 via sol-gel process, using P123, silatrane, $FeCl_3$, and Ti (IV) isoproproxide as structure-directing agent, silica, iron, and titanium sources, respectively. XRD, FE-SEM, N_2 adsorption/desorption isotherm, and DRUV were used to characterize physical properties. The catalytic activity of Fe-Ti-SBA-15 was studied on phenol hydroxylation by a high permeation liquid chromatography (HPLC), and determined the optimum conditions.

4.3 Experimental

4.3.1 Materials

Fumed silica (SiO_2, 99.8%, Aerosil®380, Nippon Aerosil Co, Ltd. Japan), titanium(IV) isopropoxide (98%, Acros organics, USA), iron(III) chloride hexahydrate ($FeCl_36H_2O$, Sigma-Aldrich, USA), triethanolamine (TEA, synthesis grade, Carlo Erba, Milan, Italy), ethylene glycol (EG, 99%, AR grade, J.T. Baker, Philipsburg, NJ), UHP grade nitrogen (N_2, 99.99% purity, Thai Industrial Gases Public Company Limited (TIG), Thailand), acetronitrile (CH_3CN, 99.9%, HPLC grade, Labscan, Bangkok, Thailand), poly(ethylene glycol)-block-poly(propylene glycol)-block-poly(ethylene glycol) ($EO_{20}PO_{70}EO_{20}$, Pluronic123 or P123, Sigma-Aldrich, Singapore), hydrochloric acid (HCl, 37%, Labscan, Thailand), catechol (CAT, 99%, Sigma-Aldrich, USA), hydroquinone (HQ, 99%, Sigma-Aldrich, USA), 1,4-benzoquinone (BQ, 98%, Sigma-Aldrich, USA), phenol detached crystals (Fisher scientific, UK), hydrogen peroxide (H_2O_2, 30% w/v, Fisher scientific, UK). All chemicals were used without further purification.

4.3.2 Precursor Synthesis

4.3.2.1 *Synthesis of Silatrane*

The silatrane precursor was synthesized from fumed silica and TEA in EG solvent. By following the method cited elsewhere [4], 18.6 g of TEA was refluxed with 6 g of fumed silica in 100 mL of EG at 200 °C under nitrogen atmosphere for 12 h using an oil bath as a heat source. Excess EG was removed under vacuum at 110 °C to obtain a crude brown solid, followed by washing with acetonitrile to remove unreacted TEA and excess EG. The white silatrane product was obtained and vacuum dried overnight in desiccator.

4.3.2.2 *Synthesis of SBA-15*

SBA-15 was synthesized at room temperature from homemade silatrane using P123 as structural directing agent in acidic conditions. The P123 (4 g) was dissolved 2M HCl (80 g, part A) and stirred for 1 h. For part B, silatrane (8.8 g) was dissolved in H_2O (20 g) and then continuously stirred for 1 h to obtain homogenous solution. The solution from part B was then poured into part A

and stirred at room temperature for 24 h; the product was recovered by filtration, washed with deionized water, and dried overnight under ambient conditions. The obtained solid was calcined at 550 °C in air for 6 h with a heating rate of 0.5 °C/min to remove the residual organics [4].

4.3.2.3 Synthesis of Ti-SBA-15

Ti-SBA-15 was synthesized from silatrane as silica source, titanium(IV) isopropoxide as titanium source, P123 as the structure-directing agent, and 2 M HCl as the acid catalyst, using various Ti/Si molar ratios (0.01, 0.03, 0.05, 0.07 and 0.09). For part A, 4 g of P123 was dissolved in 80 g of 2 M HCl and stirred until it was completely dissolved. For part B, 8.8 g of silatrane was stirred in 20 g of H_2O for 1 h or until it became homogenous solution. The solution of part B was then poured into part A. The required amount of titanium(IV) isopropoxide was added into the homogenous solution with stirring. The resulting gel was aged at room temperature for 24 h and the product was recovered by filtration, washed with deionized water, and dried overnight at ambient temperature. The products were calcined at 550 °C in air for 6 h at a heating rate of 0.5 °C/min to remove the residual organics prior to characterization [4].

4.3.2.4 Synthesis of Fe-SBA-15

Fe-SBA-15 was synthesized from silatrane and $FeCl_3$ as silica and iron sources, respectively. P123 as the structure-directing agent and 2 M HCl as the acid catalyst were added. Fe-SBA-15 with different Fe/Si molar ratios (0.01, 0.03, 0.05, 0.07 and 0.09) was prepared. For part A, 4 g of P123 was dissolved in 80 g of 2 M HCl. For part B, the required amount of $FeCl_3$ and 8.8 g of silatrane were added into 20 g of H_2O, and stirred until it was homogeneous. The solution of part B was then poured into part A. The resulting gel was aged at room temperature for 24 h and the product was recovered by filtration, washed with deionized water, and dried at ambient condition overnight. The obtained solid was calcined at 550 °C in air for 6 h with a heating rate of 0.5 °C/min to remove residual organics before characterization [15].

4.3.2.5 Synthesis of Ti-Fe-SBA-15

Ti-Fe-SBA-15 was synthesized from silatrane, titanium(IV) isopropoxide, and $FeCl_3$ as silica, titanium, and iron sources, respectively, using P123 as the structure-directing agent and 2 M HCl as acid catalyst. Ti-Fe-SBA-15 with various molar ratios of Ti/Si and Fe/Si (0.01, 0.03, 0.05, 0.07to 0.09) were prepared.

To synthesize Ti-Fe-SBA-15, 4 g of P123 was dissolved in 80 g of 2 M HCl (part A). For part B, 8.8 g of silatrane and a required amount of $FeCl_3$ were stirred in 20 g of H_2O for 1 h or until it became homogenous solution. The solution of part B was then poured into part A, followed by adding a required amount of titanium(IV) isopropoxide. The resulting mixture was aged at room temperature for 24 h to obtain crude product. The product was filtered, washed with deionized water, and dried overnight at ambient temperature, followed by calcination at 550 °C in air for 6 h at a heating rate of 0.5 °C/min to remove the residual organics before characterization.

4.3.3 Materials Characterization

The products were characterized by Small-angle X-ray scattering (SAXS) spectroscopy for phase identification of a crystalline material and information on unit cell dimensions, using Rigaku TTRAX III equipped with CuKα (λ_{av}=0.154 nm) radiation generated at 50 kV and 30 mA over the 2θ range of 0.4–5°. Wide Angle X-Ray Diffraction (WAXD) was performed on a Rigaku Smartlab® with a scanning speed of 10 °/min and CuKα source (λ= 0.154 Å) in a range of 2θ = 20–80° to determine the metal nanocrystals. Field emission scanning electron microscopy (FESEM, JSM-7001F) was used to collect secondary electron images from powder mounted on double-sided carbon tape using a Zeiss Ultra plus and operating at 0.3–0.5 kV to minimize charging. Nitrogen adsorption and desorption isotherms were measured at -196 °C after outgassing at 250 °C for 12 h under vacuum (Quantasorb JR, Mount Holly, NJ) to determine the Brunauer–Emmett–Teller (BET) specific surface area. The pore size distributions were obtained from the adsorption and desorption branches of the nitrogen isotherms by the Barrett-Joyner-Halenda method. Thermal properties were analyzed by Thermal gravimetric

analysis-Fourier transform infrared spectrometry (TGA-FTIR) on Pyris Diamond Perkin Elmer using a heating rate of 10 °C/min under N_2 atmosphere. FTIR analysis was conducted on a vector 3.0 Bruker Instrument (Equinox 55) with a scanning resolution of 4 cm^{-1} to investigate functional groups of the synthesized precursors. Powder specimens contained 1.0% sample with 99% potassium bromide (KBr). Diffuse reflectance UV-visible (DRUV) spectroscopic measurements were carried out on a Shimadzu UV-2550 spectrophotometer recorded from 200 to 900 nm and using $BaSO_4$ as a reference. It was used for identification and characterization of metal ion coordination in- or extra-framework of SBA-15 after calcination. The metal contents in samples were observed by X-ray fluorescence (XRF) on AXIOS PW 4400.

4.3.4 Phenol Hydroxylation Procedure

The procedure was followed Adam and coworkers' method for the oxidation of phenol by dissolving phenol (1.88 g, 20 mmol) in 10 mL of water [12]. Then, the mixture was poured into a bottle containing 30 mg of catalyst and immersed in an oil bath at 30°C with continuous stirring. After the reaction temperature was stabilized, H_2O_2 (2.27 ml, 20 mmol) was added into the reaction mixture. Aliquots of the reaction mixture (0.5 cm^3) were periodically withdrawn using a syringe. All samples were investigated by HPLC. All reactions were repeated three times and average values were used in the data presentation.

4.3.5 Leaching and Reusability of the Catalyst

Leaching of metal ion from the catalyst was determined by filtering off the catalyst from the reaction mixture after 5 min. The filtrate was transferred without delay into the round bottom flask which had been controlled at the same temperature. The reaction was allowed to continue for an additional 20 min (without the catalyst) and the course of the reaction was monitored periodically by HPLC-UV to compare with the results before filtration [12].

Reusability was studied by regenerating the catalyst by washing with distilled water, dried in an oven at 353K for 6 h and calcined at 500 °C for 2 h with heating rate at 0.5 °C/min. The catalyst was collected and reused for further runs, as described earlier [12].

4.4 Results and Discussion

4.4.1 Characterization of Silatrane Precursor

Silatrane was synthesized via the Oxide One Pot Synthesis (OOPS) process. Thermal property of obtained product was investigated by TGA in Figure 4.1. There was major weight loss at about 350 °C that was corresponding to the loss of organic parts. The remaining ash was 19.02% that was close to the theoretical ceramic yield (18.63%). Thus, its corresponding structure is referring to that shown in Figure 4.2. The FT-IR result is exhibited in Figure 4.3. The FT-IR result showed the peaks at 3000-3700 cm^{-1} (w, υO-H), 2860-2986 cm^{-1} (s, υC-H), 1244-1275 cm^{-1} (m, υC-N), 1073 cm^{-1} (s, υC-O), 1049 cm^{-1} (s, υSi-O), 1021 cm^{-1} (s, υC-O), 785 and 729 cm^{-1} (s, υSi-O-C), and 579 cm^{-1} (w, υN-Si) [4].

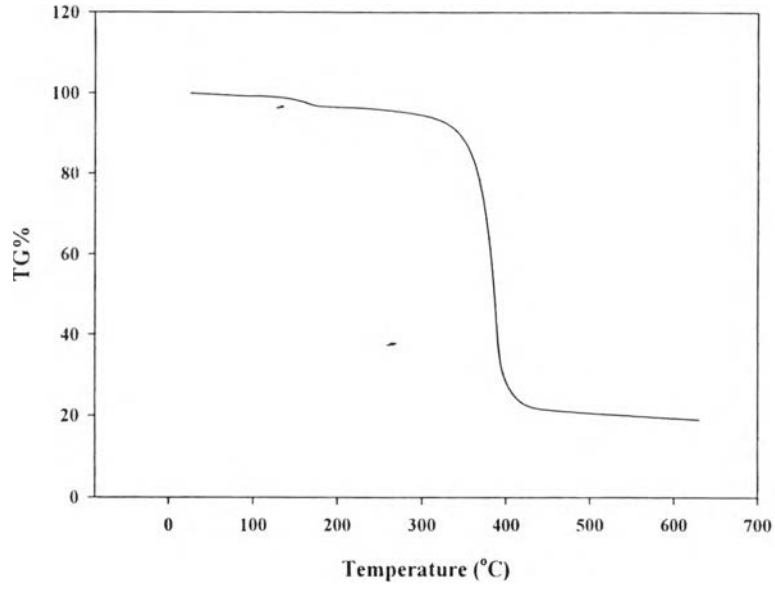

Figure 4.1 TGA thermogram of silatrane precursor.

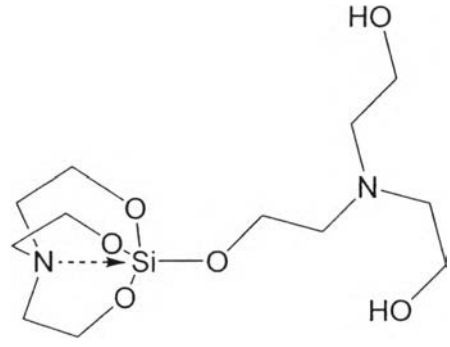

Figure 4.2 The structure of silatrane.

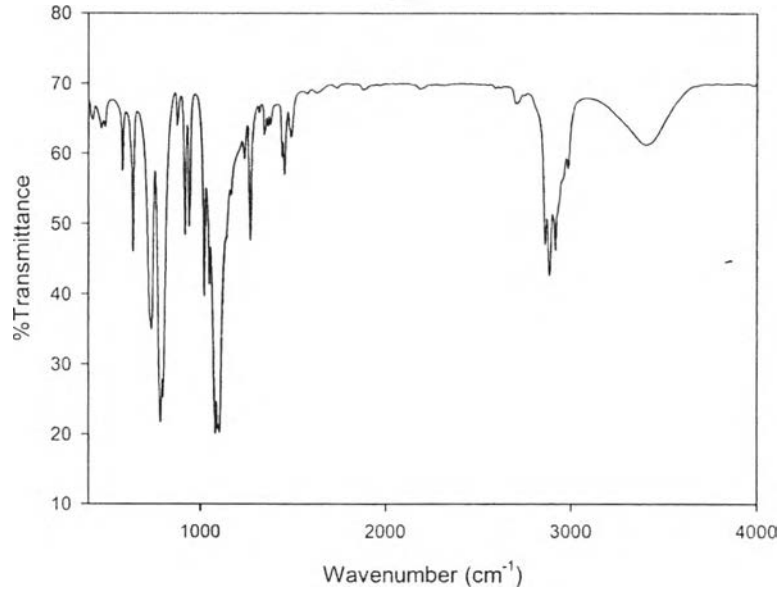

Figure 4.3 FT-IR spectra of silatrane.

4.4.2 Characterization of Fe-SBA-15 Catalyst

Fe-SBA-15 was also synthesized via the sol-gel process. The obtained product was white powder. The SAXS patterns of calcined SBA-15 and Fe-SBA-15 containing different amount of Fe loadings were shown in Figure 4.4. All samples exhibited three well resolved reflection peaks at (100) with higher intensity and (110) along with (200) consistent with the hexagonal space group of p6mm [6]. The

increasing of the peak intensity at (100) was observed with the increasing of the Fe/Si ratio. Li and coworkers found that iron ion could partly improve the structure ordering by hydrolyzing the iron precursors ($FeCl_36H_2O$) and producing protons, as shown in eq. 4.1 [5, 8]. These protons played the important role in the SBA-15 formation through the $(S^0H^+)(X^-I^0)$ pathway where S^0 is the non-ionic surfactant (P123), I^0 is the protonated silanol group, H^+ is proton, and X^- is the counteranion [3].

$$Fe^{3+} + 2H_2O \rightarrow Fe(OH)_2^+ + 2H^+ \qquad 4.1\ [8]$$

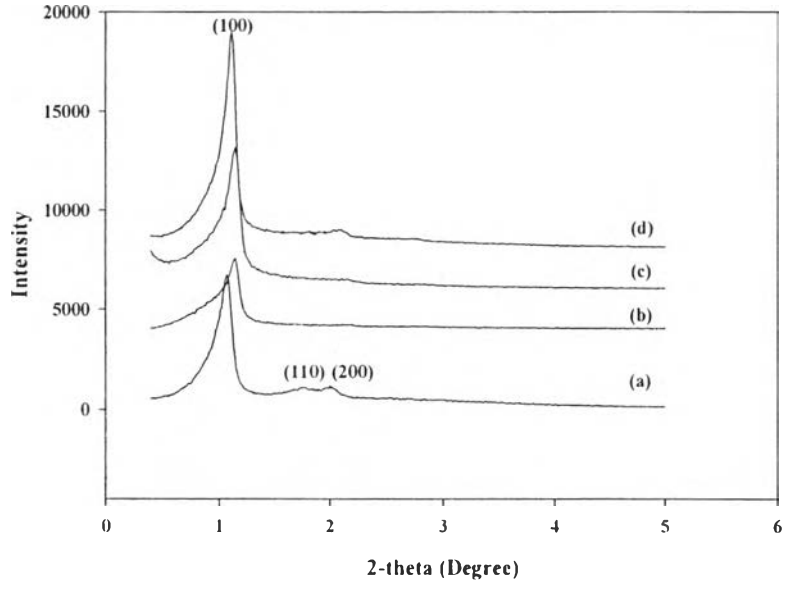

Figure 4.4 The SAXS patterns of SBA-15 (a) and Fe-SBA-15 containing different Fe/Si mol ratios of b) 0.01, c) 0.03, and d) 0.05.

However, this tendency is destroyed when the Fe/Si ratio above 0.05 probably due to the iron accumulation, causing less distribution Furthermore, the Fe-O bond length (0.197 nm) is longer than Si-O bond length (0.161 nm) [6]. Thus, the structures of framework become less order when adding higher amount of iron contents. Moreover, when adding the higher amount of iron contents, the XRD peaks were shifted to the higher two-theta with narrower d-spacing between lattices probably due to the distortion of the SBA-15 structure, consistent with the FE-SEM images in Figure 4.8.

DR-UV results showed the ligand-metal charge transfer between tetrahedral oxygen ligands and central Fe^{3+} ion. The spectra of the calcined Fe-SBA-15 containing different amounts of Fe loading are shown in Figure 4.5. There are two strong absorption bands at 210 and 250 nm, associating with the d_n–p_n charge-transfer transition between the iron (Fe^{3+}) and tetrehedral oxygen atoms in the framework of Fe-O-Si in tetrahedral geometry $[FeO_4]^-$[5]. Moreover, the energy band gap of the iron in the silica framework calculated from equation 4.2 using the DRUV results was equal to 7.95×10^{-19} Joules or 4.97 eV.

$$E = h \times \frac{c}{\lambda} \qquad 4.2$$

Where h = Planks constant = 6.626×10^{-34} Joules sec

C = Speed of light = 3.0×10^{8} meter/sec

λ = Wavelength that gives the highest intensity = 250×10^{-9} meters

1 eV = 1.6×10^{-19} Joules (conversion factor)

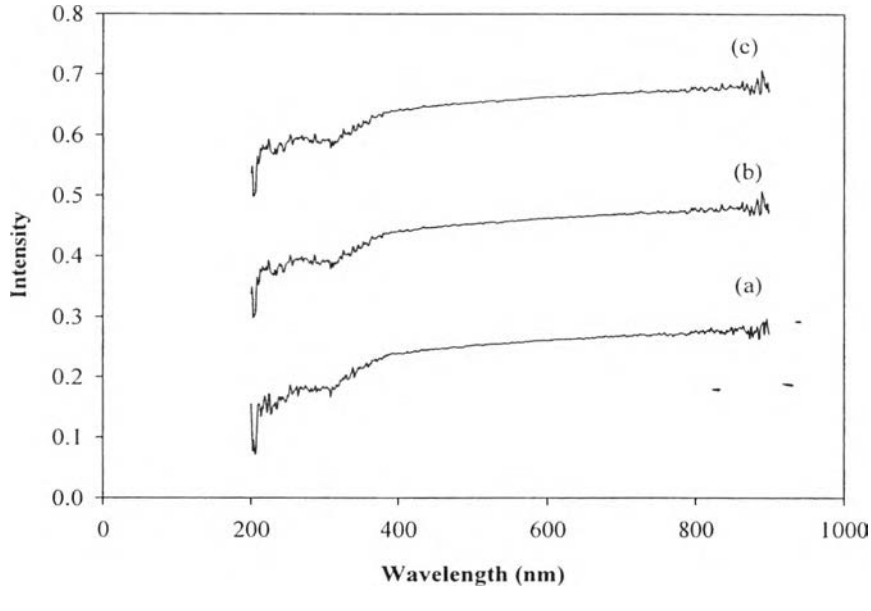

Figure 4.5 The DRUV spectra of the calcined Fe-SBA-15 containing different Fe/Si mol ratios of a) 0.01, b) 0.03, and c) 0.05.

N_2 adsorption and desorption isotherms of SBA-15 and Fe-SBA-15 with different Fe contents are shown in Figure 4.6. All samples showed type IV isotherm with broad H1 type hysteresis loop, which is typical for porous materials with uniform pore [16]. The pore size distributions derived from BJH desorption are shown in Figure 4.7 (~4-6 nm). There was the well-defined steep parallel step at relative pressure at 0.5-0.7 related to capillary condensation of N_2 within the uniform pores. According to Table 4.1, BET surface area, pore volume, and average pore diameter slightly change when adding iron into the SBA-15 framework.

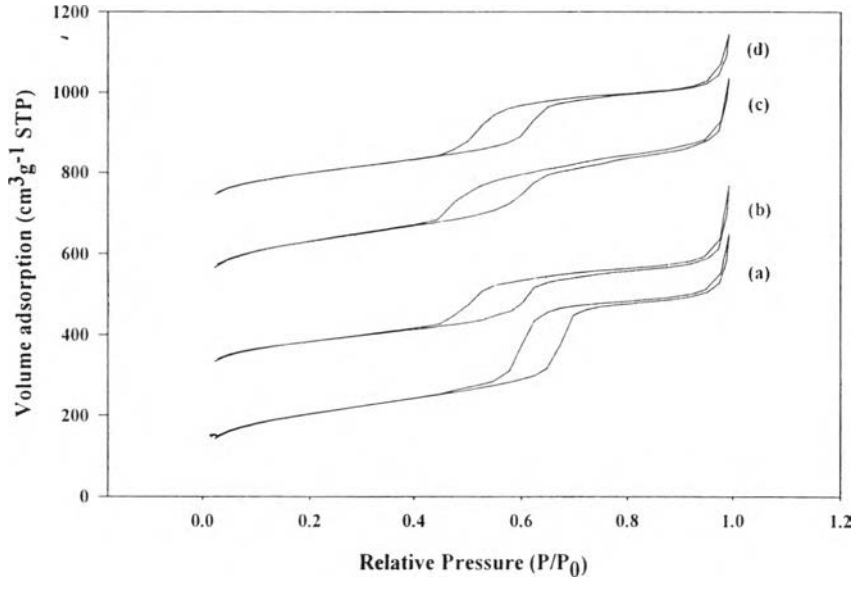

Figure 4.6 N_2 adsorption–desorption isotherms of SBA-15 a) and Fe-SBA-15 with different Fe contents of b) 0.01, c) 0.03, and d) 0.05.

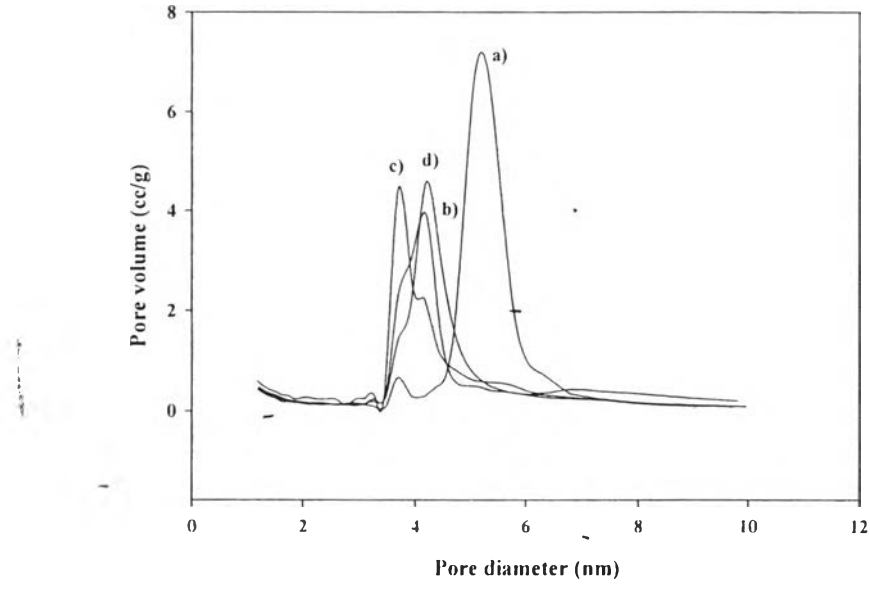

Figure 4.7 The pore size distribution by BJH desorption of SBA-15 a) and Fe-SBA-15 with different Fe contents of b) 0.01, c) 0.03, and d) 0.05.

Table 4.1 BET surface area, pore volume, and average pore diameter of xFe-yTi-SBA-15 samples

Sample	BET surface area (m^2/g)	Pore volume (cc/g)	Average pore diameter (nm)
SBA-15	690	0.897	5.21
0.01 Fe-SBA-15	604	0.772	5.11
0.03 Fe-SBA-15	763	0.899	4.71
0.05 Fe-SBA-15	665	0.759	4.57
0.01 Ti-SBA-15	761	0.971	5.11
0.03 Ti-SBA-15	702	0.951	5.10
0.01Ti-0.01Fe-SBA-15	631	0.621	3.933

XRF results in Table 4.2 indicated that the actual contents of iron and titanium in the products were less than in the gel composition probably owing to the strong acid condition promoting the M-O-Si dissociation and giving not enough time for metal to incorporate in the framework [5].

Table 4.2 XRF data of Ti-SBA-15, Fe-SBA-15, and bimetallic Ti-Fe-SBA-15

Sample	Fe/Si (mole ratio)		Ti/Si (mole ratio)	
	Gel	Product*	Gel	Product*
SBA-15	0	0	0	0
0.01Fe-SBA-15	0.01	0.0002.	0	0
0.03Fe-SBA-15	0.03	0.0003	0	0
0.05Fe-SBA-15	0.05	0.0003	0	0
0.01Ti-SBA-15	0	0	0.01	0.0006
0.03Ti-SBA-15	0	0	0.03	0.0017
0.01Ti-0.01Fe-SBA-15	0.01	0.0002	0.01	0.0005

Morphologies of pure SBA-15 and iron containing SBA-15 by FE-SEM are shown in Figure 4.8. It was found that pure SBA-15 and SBA-15 with different iron loadings were rod-like [17]. However, the morphology of 0.01 Fe-SBA-15 was not smooth at the surface. This caused the small angle x-ray pattern of 0.01Fe-SBA-15 become less order that was shown in Figure 4.4.

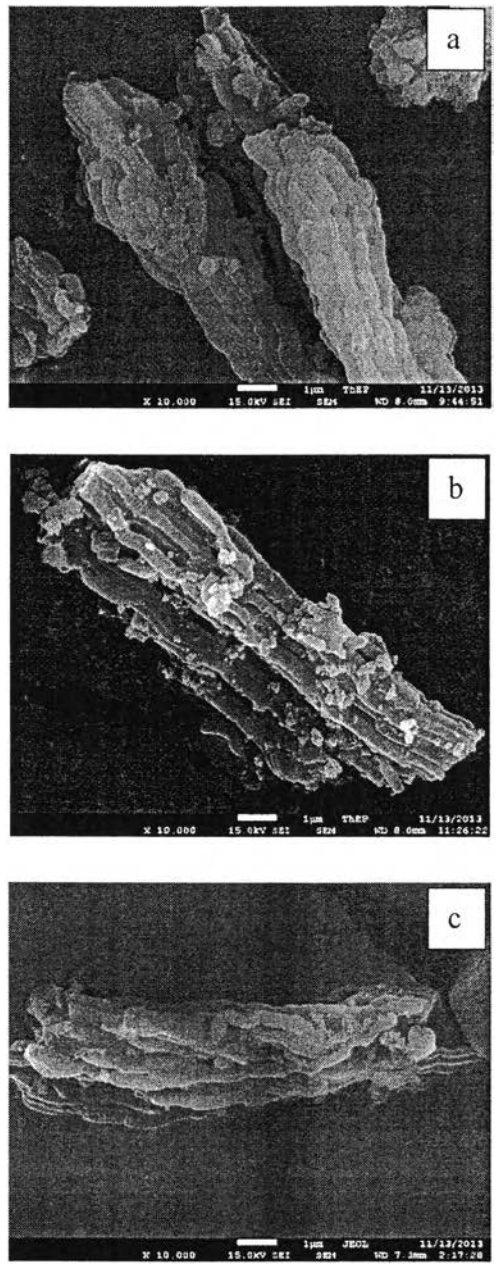

Figure 4.8 FE-SEM images of a) SBA-15, b) 0.01 Fe-SBA-15, c) 0.05 Fe-SBA-15.

4.4.3 Characterization of Ti-SBA-15 Catalysts

Ti-SBA-15 synthesized via the sol-gel process was white powder. The SAXS patterns of calcined SBA-15 and Ti-SBA-15 containing different amounts of Ti loading are shown in Figure 4.9. All samples exhibited three reflection peaks at (100), (110), and (200), respectively, consistent with the 2D hexagonal space group *p6mm* [6]. Since, the condition of SBA-15 synthesis was highly acidic condition;

therefore, it was difficult for titanium to incorporate into the framework of SBA-15 [8]. Moreover, the radius of Ti^{4+} ion (60.5 pm) [8] was larger than that of Si^{4+} ion (54 pm), thus, when Ti was incorporated into the SBA-15 framework, it destroyed some structures of SBA-15, causing the decrease in all peaks.

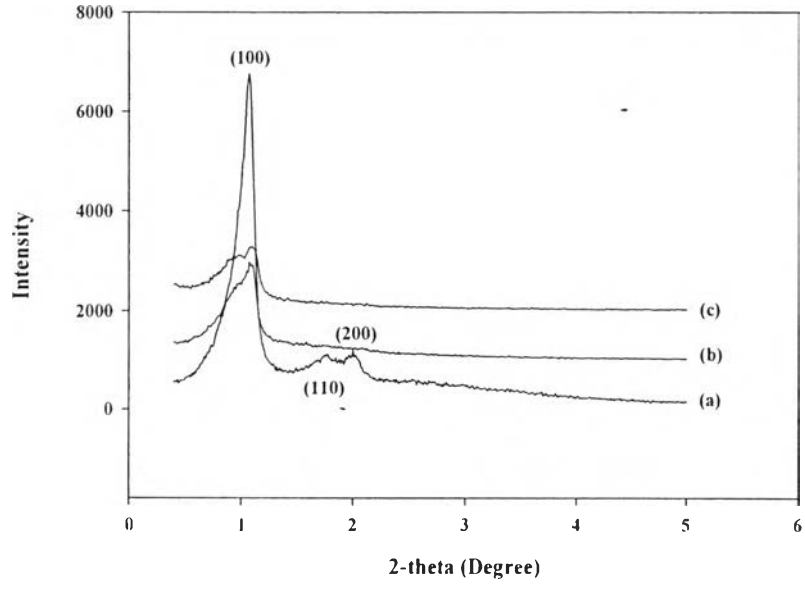

Figure 4.9 SAXS patterns of the calcined pure SBA-15 and Ti-SBA-15 containing different amount of Ti loadings (Ti/Si mol ratio): (a) 0, (b) 0.01, and (c) 0.03.

DRUV spectra of the calcined Ti-SBA-15 containing different amounts of Ti loading are shown in Figure 4.10. It was found that there was the broad band center at 220 nm in all samples displaying a low-energy d_{π}–p_{π} charge-transfer transition between tetrahedral oxygen ligands and central Ti^{4+} ion. This band implied to the tetracoordinated Ti(IV) ion in the silica framework [8], confirming that Ti was incorporated into the silica framework. Moreover, the energy band gap of the titanium in the silica framework calculated from equation 4.2 using the DRUV results with the highest intensity wavelength (λ) of 215 x 10^{-9} meters was equal to 5.79 x 10^{-19} Joules or 5.79 eV.

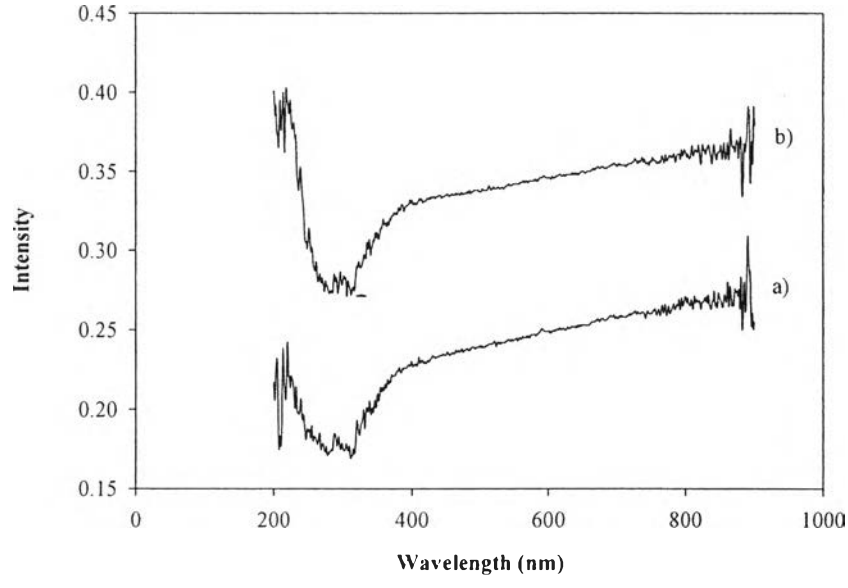

Figure 4.10 The DRUV spectra of the calcined Ti-SBA-15 containing different amounts of Ti loadings: a) 0.01 and b) 0.03.

From Figure 4.11, all Ti-SBA-15 samples showed the type IV isotherms with broad H1 type, according to IUPAC, that displayed the typical mesoporous materials. There was steep parallel step at relative pressure of 0.5–0.7, the characteristic of the capillary condensation of N_2. The pore size distribution of Ti-SBA-15 was about ~4–5nm (Figure 4.12). The BET surface area, pore volume and average pore diameter are summarized in Table 4.1. It was found that the surface area, pore volume and pore diameter increased when compared to pure SBA-15 since ion radius of Ti^{4+} (60 pm) [8] was larger than that of Si^{4+}. Thus, when Ti was incorporated into the silica framework, it can increase surface area, pore volume and pore diameter. However, titanium containing SBA-15 was less order than pure SBA-15 in accordance with the small angle XRD patterns shown Figure 4.9.

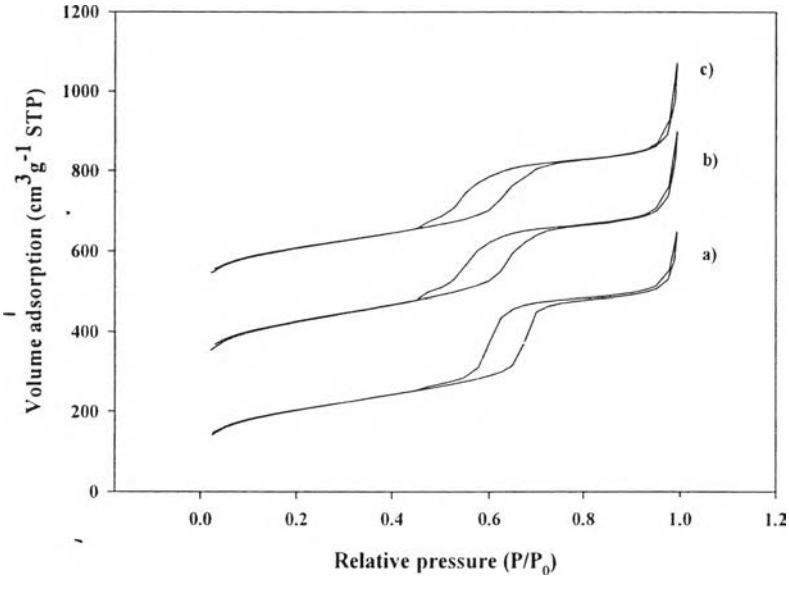

Figure 4.11 N_2 adsorption–desorption isotherms of a) SBA-15, b) 0.01 and c) 0.03 Ti-SBA-15.

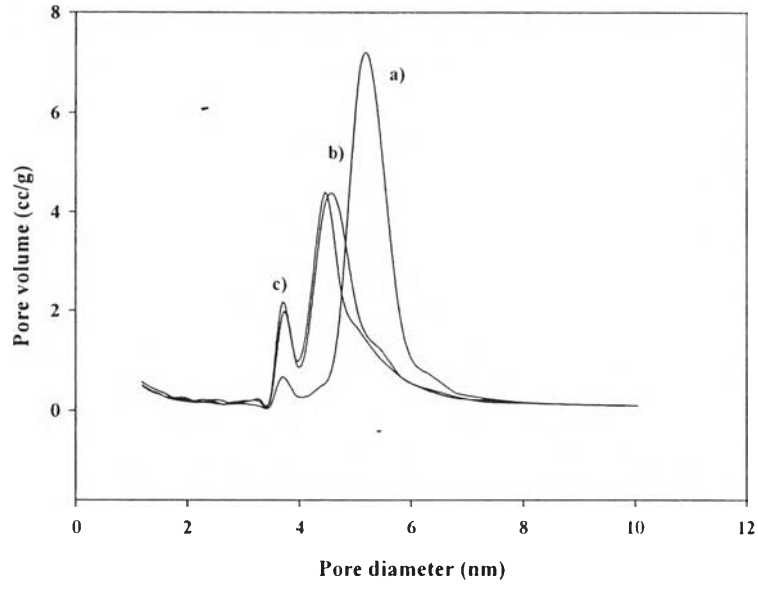

Figure 4.12 Pore size distribution by BJH desorption of a) SBA-15, b) 0.01 and c) 0.03Ti-SBA-15.

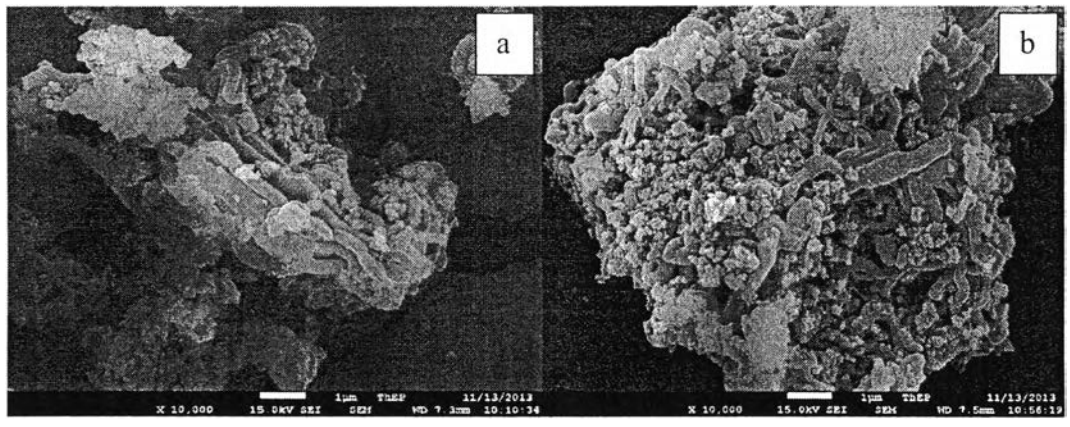

Figure 4.13 FE-SEM images of a) 0.01 Ti-SBA-15 and b) 0.03 Ti-SBA-15.

The morphology of 0.01Ti and 0.03 Ti-SBA-15 were shown in Figure 4.13. It showed that when higher amount of titanium were added into the system. The morphology became less tubular arrangement.

4.4.4 Characterization of Fe-Ti-SBA-15 Catalysts

Bimetallic Fe-Ti SBA-15 product was also white powder. The small angle XRD patterns in Figure 4.14 showed similar results to the mesoporous silica SBA-15, giving three peaks at (100), (110), and (200). These peaks are the characteristic peaks of mesoporous material with 2D-hexagonal structure.

Figure 4.15 shows a broad band between 200 and 350 nm centered at 220 and 255 nm, assigned to the low-energy d_{π}–p_{π} charge-transfer transitions between tetrahedral oxygen ligands and central Ti^{4+} and Fe^{3+} ions. These two bands referred to tetrahedral Ti(IV) and Fe(III) ions in the framework of the mesoporous silica [8]. However, the bands at 270 and 480 nm corresponded to partially polymerized octahedral Ti and Fe species were not detected, implying that no extraframework or M-O-M cluster occurs.

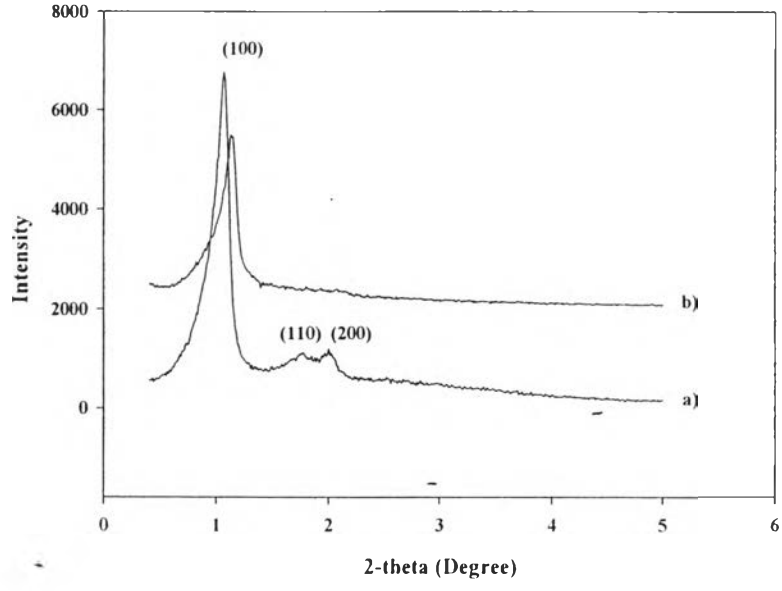

Figure 4.14 The SAXS patterns of a) SBA-15 and b) 0.01Fe-0.01Ti-SBA-15.

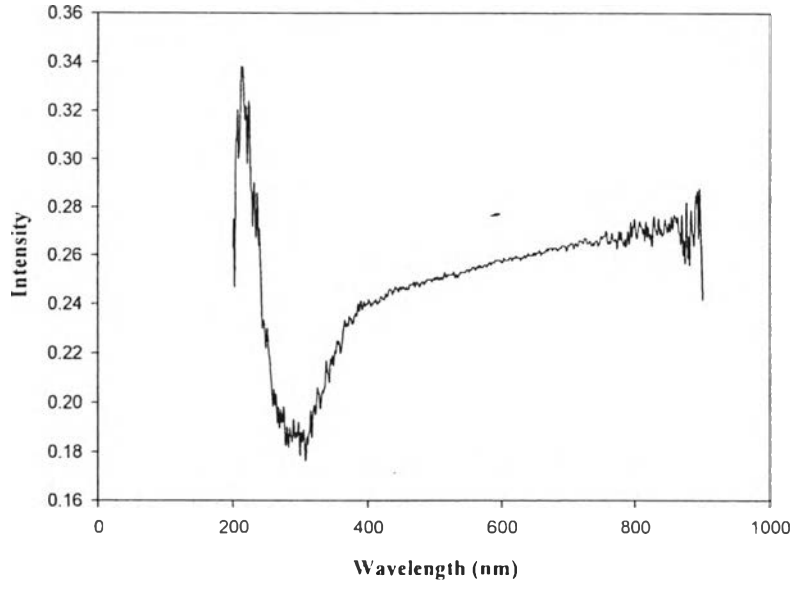

Figure 4.15 The DRUV spectrum of the calcined 0.01Fe-0.01Ti-SBA-15.

Figure 4.16 shows the N_2 adsorption-desorption isotherms of pure SBA-15 and 0.01Fe-0.01Ti-SBA-15. It was found that bimetallic 0.01Fe-0.01Ti was also of type IV with H1 hysteresis loop with narrow pore size distribution. The peak was broader when compared to pure-SBA-15. It could be meant that the structure was not uniform, in accordance with the results from the N_2 adsorption-desorption isotherm. The pore size distribution of 0.01Fe-0.01Ti-SBA-15 was about 4 nm, as shown in Figure 4.17. Furthermore, the BET surface area, pore volume and average pore size decreased when compared to pure SBA-15.

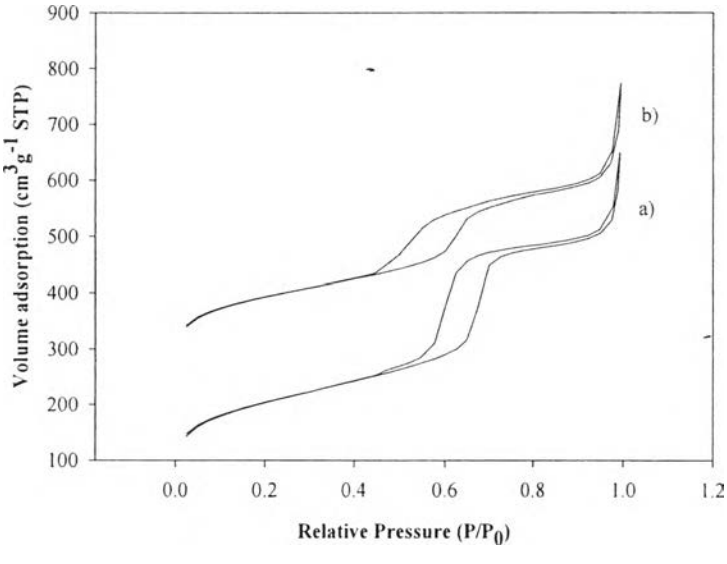

Figure 4.16 N_2 adsorption–desorption isotherms of a) SBA-15 and b) 0.01Fe-0.01Ti-SBA-15.

The morphology of 0.01Fe-0.01Ti-SBA-15 in Figure 4.18 shows the bundle of tubular arrangement like pure SBA-15. It means that 0.01Fe-0.01Ti-SBA-15 still maintained their structure after adding low amount of metal in the system.

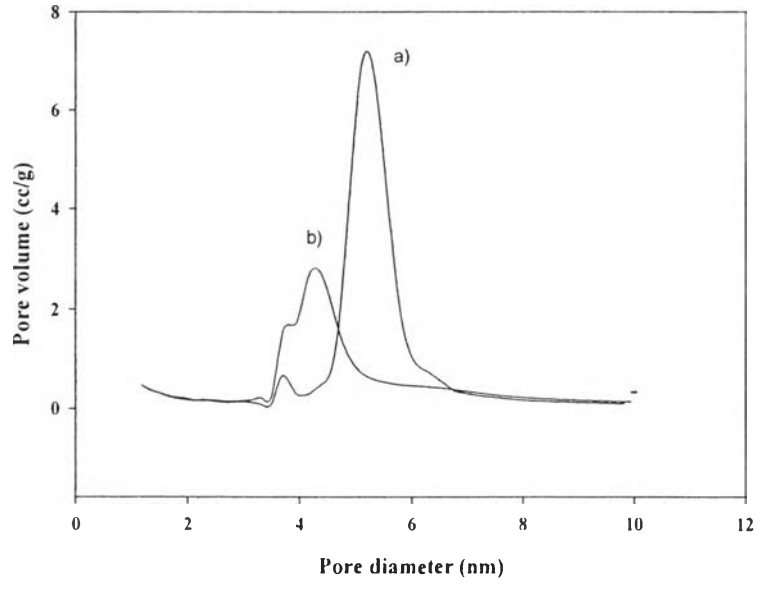

Figure 4.17 Pore size distribution by BJH desorption of a) SBA-15 and b) 0.01Ti-0.01Fe-SBA-15.

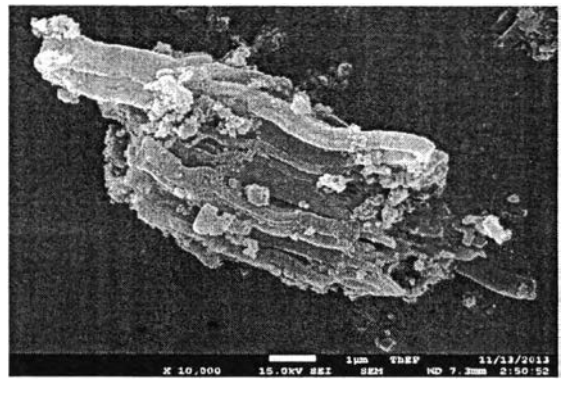

Figure 4.18 FE-SEM image of 0.01Fe-0.01Ti-SBA-15.

4.4.5 Catalytic Activity on Phenol Hydroxylation

All synthesized samples were studied on the phenol hydroxylation. They were investigated on the effects of reaction temperature, reaction time, molar

ratio of reactants (phenol:H_2O_2), catalyst content, and metal loading to obtain the optimal condition for phenol hydroxylation.

4.4.5.1 The Effects of Reaction Temperature and Time

The optimal time and temperature were studied by using 30 mg of 0.01Fe-0.01Ti-SBA-15 with 1:1 phenol (1.9 g, 20 mmol):H_2O_2 (2.3 ml, 20 mmol) dissolving in 10 ml of water. All samples were collected at 10, 20, 30 min, 1, 2, 3, 4, and 5 h over different temperatures of 30, 50, 70, and 90 °C, as shown in Figure 4.19. It was observed that the maximum phenol conversion of 38% was obtained at 30 °C for 20 min, giving BQ as the only product. This is indicative of an excellent selectivity [14]. However, when increasing the temperature, the conversion decreased [9] due to the more H_2O_2 decomposition that reduced the efficiency of H_2O_2. Moreover, when the reaction time is prolonged the conversion also decreased probably due to the blockage of the pore or active sites by the product during the reaction [12, 14, 18]. Thus, the temperature of 30 °C for 20 min reaction time was selected as the optimum conditions for further study.

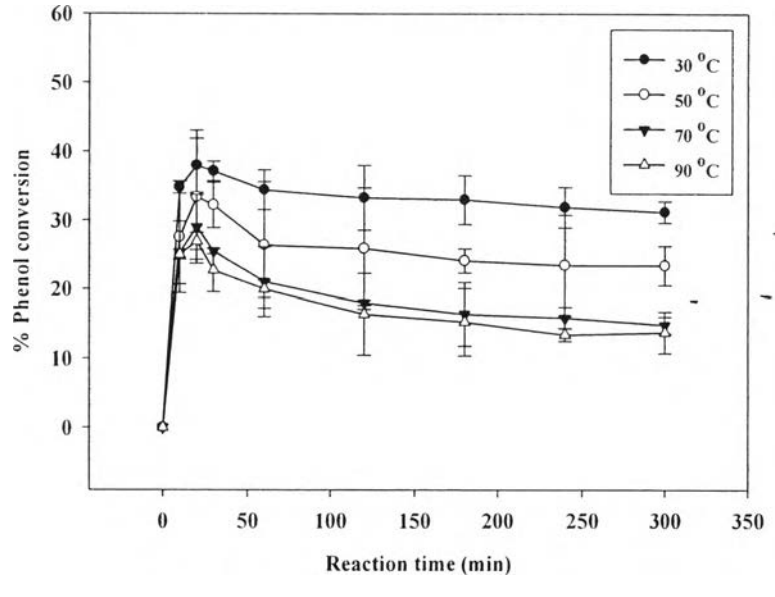

Figure 4.19 Effect of the reaction temperature and time on the phenol conversion using 30 mg of 0.01Fe-0.01Ti-SBA-15 and 1:1 phenol:H_2O_2 ratio.

4.4.5.2 The Effect of Catalyst Content

The catalyst content effect was studied using the catalyst amount ranging from 10 to 70 mg. The phenol conversion in Figure 4.20 shows that the maximum phenol conversion obtained was 37.96% when using 30 mg of catalyst. However, further increasing in the amount of catalyst to 70 mg, the conversion decreased to 28.17%. This might be that a larger amount of the catalyst, having a higher surface area, caused a more dissociation of the H_2O_2 that affected the oxidation [12, 18]. Thus, 30 mg of the catalyst content was chosen for the next study.

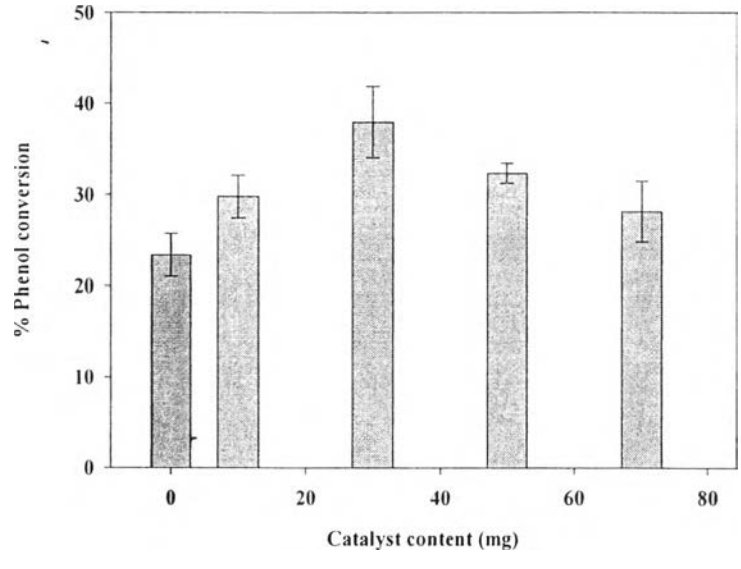

Figure 4.20 Effect of the catalyst content on the phenol conversion performed at 30 °C using 0.01Fe-0.01Ti-SBA-15 and 1:1 phenol: H_2O_2 ratio.

4.4.5.3 The Effect of Phenol:H_2O_2 Molar Ratio

There were 4 phenol: H_2O_2 molar ratios (1:1, 1:2, 1:3, and 2:1) studied (Figure 4.21). It was found that 1:1 phenol:H_2O_2 gave the highest phenol conversion at 37.96%. This ratio could be a proper ratio for H_2O_2 to freely coordinate to metal and decompose to form $OH^{\cdot}$ radical [19]. When increasing the amount of H_2O_2, the conversion decreased. As discussed previously, too much H_2O_2 resulted in too much active intermediate that affected the conversion [20]. When H_2O_2 was fixed

and the amount of phenol was increased, the conversion decreased as well. This is due to the inadequate amount of H_2O_2 to generate active species to react with the excess amount of phenol. Moreover, only BQ product was obtained in this case since H_2O_2 has difficulties to access the pores blocked by too much amount of phenol, thus, resulting in the overoxidation of product to BQ.[19, 21]. Thus, the optimum molar ratio selected was 1:1 phenol: H_2O_2.

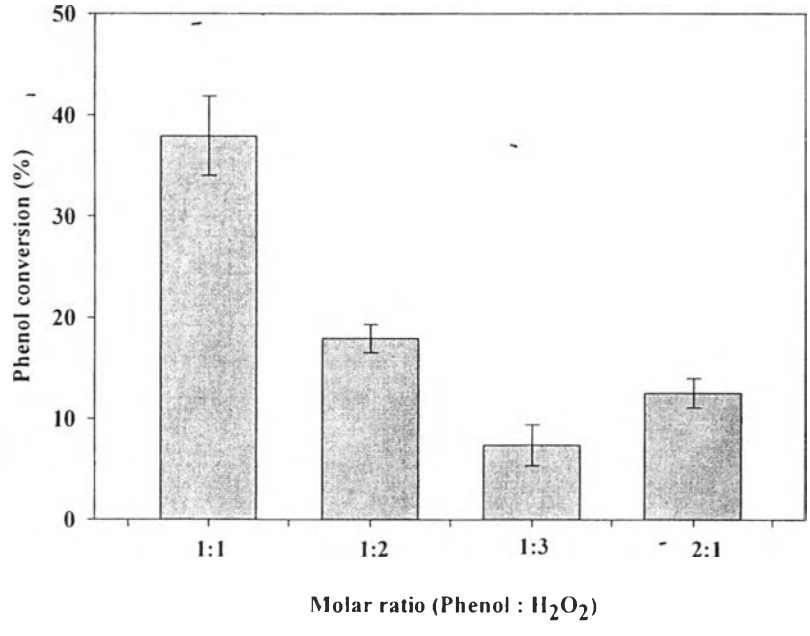

Figure 4.21 Effect of the phenol:H_2O_2 molar ratio performed at 30 °C using 30 mg of 0.01Fe-0.01Ti-SBA-15.

4.4.5.4 The Effect of the Metal Content Loaded

The effect of the metal content loaded was studied using the optimum reactions previously found. All metal loaded SBA-15 samples exhibited higher phenol conversion than the pure SBA-15, except 01Ti-0.01Fe-SBA-15 giving the highest conversion of 37.96%, as shown in Table 4.2.

Table 4.3 Effect of the metal loaded on phenol hydroxylation (Thermal reaction) at 30 °C for 20 min using 30 mg of catalyst and 1:1 phenol: H_2O_2 ratio

Samples	conversion	Selectivity		
		HQ	CAT	BQ
SBA-15	24.12±2.46	-	-	100
0.01-Fe-SBA-15	25.41±2.72	-	-	100
0.03-Fe-SBA-15	28.03±2.06	-	-	100
0.05-Fe-SBA-15	25.05±1.36	-	-	100
0.01-Ti-SBA-15	25.40±0.38	-	-	100
0.03-Ti-SBA-15	29.35±4.79	-	-	100
0.01Fe-0.01Ti-SBA-15	37.96±3.90	-	-	100
No H_2O_2	0.00	-	-	-
No Catalyst	23.37±2.38	-	-	100

4.4.5.5 Hydrothermal Stability

0.01Fe-SBA-15, 0.01Ti-SBA-15, and 0.01Fe-0.01Ti-SBA-15 were used to study the hydrothermal stability of the catalyst. After the phenol hydroxylation, all catalysts were purified with water and calcined at 500 °C with a heating rate of 0.5 °C/min for 2 h to get rid of all orgainic residues. The calcined catalysts were characterized by SAXD and SAA, as shown in Figure 4.22 and Table 4.4. It was found that from SAXD showed all calcined catalysts still maintain their structure. However, the result from SAA showed that the BET surface area, pore volume, and pore size slightly decreased.

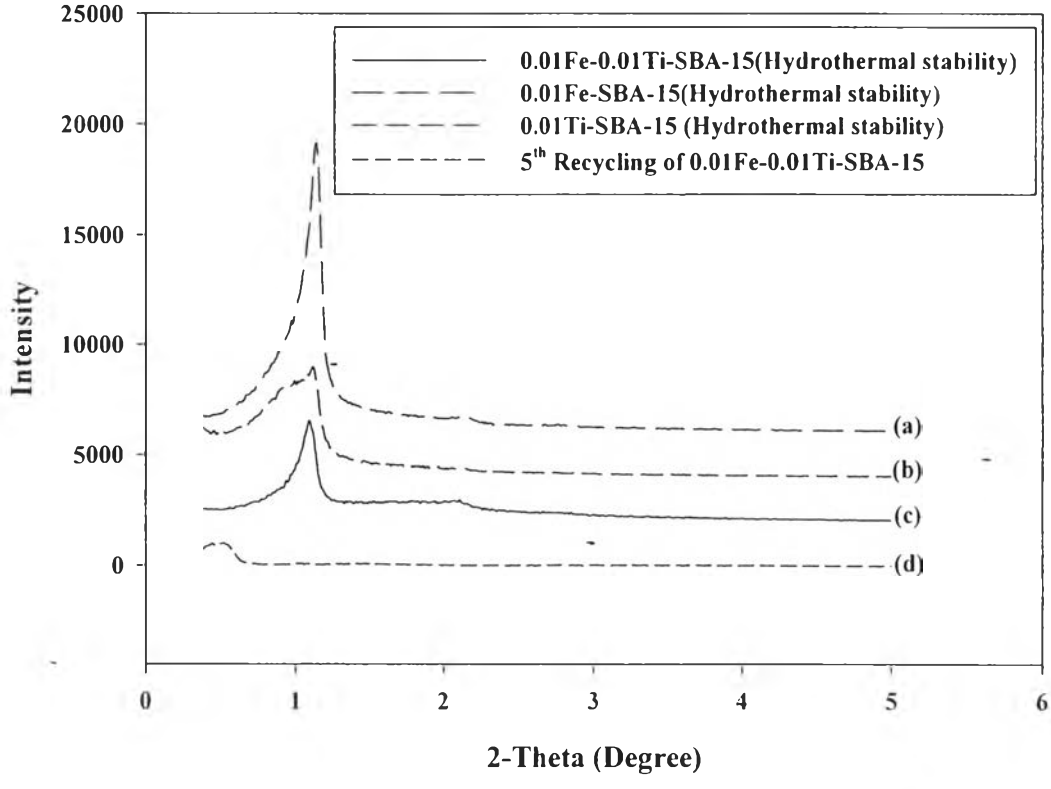

Figure 4.22 SAXD of the catalysts after used and calcined.

Table 4.4 Physical properties of the catalysts after used and calcined at 30 °C for 20 min using 30 mg of catalyst and 1:1 phenol:H_2O_2 ratio

Sample	BET Surface Area (m^2/g)	Pore Volume (cc/g)	Average Pore Size (nm)
0.01Fe-0.01Ti-SBA-15 (Hydrothermal)	540	0.73	5.43
0.01Fe-SBA-15 (Hydrothermal)	531	0.66	5.00
0.01Ti-SBA-15 (Hydrothermal)	616	0.87	5.67
0.01Fe-0.01Ti-SBA-15 (5^{th} Recycling)	464	0.99	6.08

4.4.5.6 Leaching and Reusability of the catalyst

0.01 Fe-0.01Ti-SBA-15 was used to study the leaching by removing from the reaction mixture after 5 min and allowing the reagents to continue the reaction. The conversion result was slightly constant after the removal of catalyst, as shown in Table 4.5. That means, no leaching of metal ion during phenol hydroxylation occurred [12].

Table 4.5 Study on the catalyst leaching of bimetallic 0.01Fe-0.01Ti-SBA-15 at 30 °C for 20 min using 30 mg of 0.01Fe-0.01Ti-SBA-15 and 1:1 phenol: H_2O_2 ratio

Time	Conversion (%)	Selectivity (%)		
		HQ	CAT	BQ
5 min	11.89±1.12	-	-	100
10 min	10.74±1.53	-	-	100
15 min	10.33±2.65	-	-	100
20 min	9.76±1.36	-	-	100

For the reusability study of the 0.01Fe-0.01Ti-SBA-15 catalyst, the catalyst was calcined prior to reuse to get rid of all residues blocking the active sites [22]. As can be seen in Table 4.6, after the catalyst was reused for 5 times, the conversion decreased, consistent to the result from SAXD showing that this catalyst could not maintain the structure (Figure 4.22), since the structure was destroyed [22].

4.4.5.7 Proposed Mechanism of the Catalytic Reaction

Several researchers have proposed the phenol hydroxylation by using H_2O_2 as an oxidizing agent. The reaction was related to a free radical mechanism which exhibited the formation of benzoquinone [6, 12]. The solvent played an important role in the formation of the free radical intermediate [19].

Table 4.6 Study on the reusability of bimetallic 0.01Fe-0.01Ti-SBA-15 at 30 °C for 20 min using 30 mg of 0.01Fe-0.01Ti-SBA-15 and 1:1 phenol:H_2O_2 ratio

No. of Recycling	Conversion (%)	Selectivity (%)		
		HQ	CAT	BQ
#1	20.19±2.59	-	-	100
#2	16.34±2.87	-	-	100
#3	15.84±2.68	-	-	100
#4	16.91±3.08	-	-	100
#5	10.95±0.47	-	-	100

In this reaction, water was used as solvent, which is considerably safer, cheaper, and more environmentally benign than other organic solvents. Furthermore, the phenol conversion also increased when the polarity of solvent increased and water resulted in the highest conversion, giving BQ as the only product [18, 23]. In the free radical mechanism, there are two competitive reactions for OH radical: In the case of high concentration of H_2O_2, H_2O_2 preferred to be decomposed to form water and oxygen (see step 3, Figure 4.23), causing a low conversion of phenol. On the other hand, in a low concentration of H_2O_2 system, OH radical is reacted with phenol to form product as CAT, HQ, and BQ, see step 2, in Figure 4.23 [12].

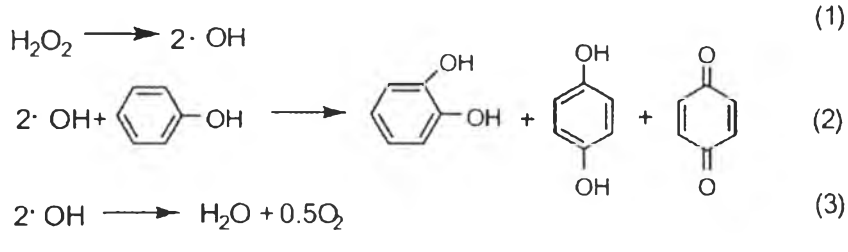

Figure 4.23 Common reaction mechanism for the formation of diphenol in phenol hydroxylation [12].

For the active sites of iron, it was believed to have a mechanism shown in Figure 4.24.

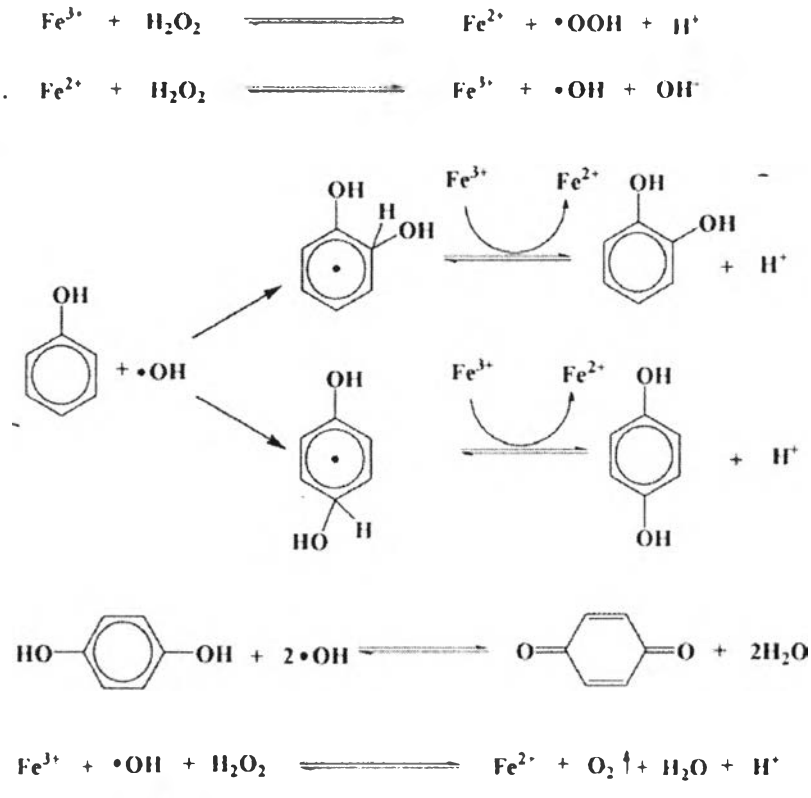

Figure 4.24 Phenol hydroxylation reaction pathway of Fe ions [24].

For the active sites of titanium, it was believed to have a mechanism as follows. In protic solvents, the mechanism of phenol hydroxylation to HQ is shown in Figure 4.25 [21].

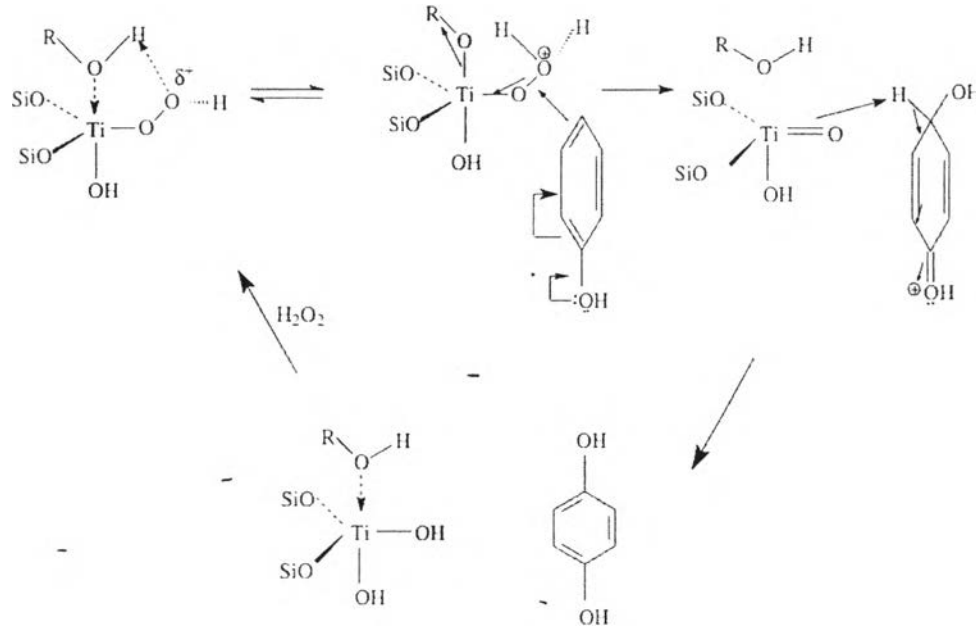

Figure 4.25 The mechanism of phenol hydroxylation to HQ via titanium [21].

In protic solvents, the mechanism of phenol hydroxylation to CAT-is shown in Figure 4.26 [21].

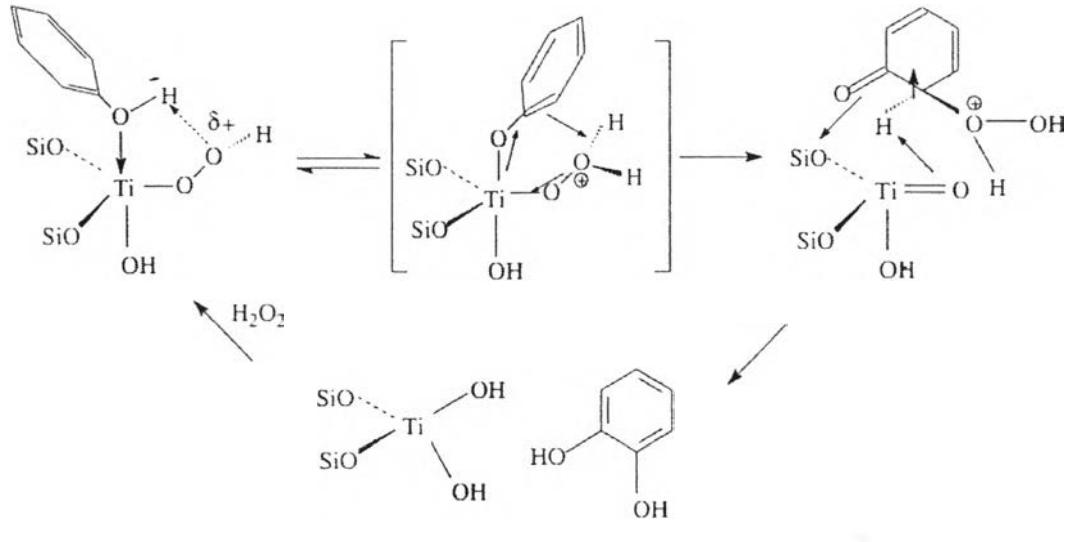

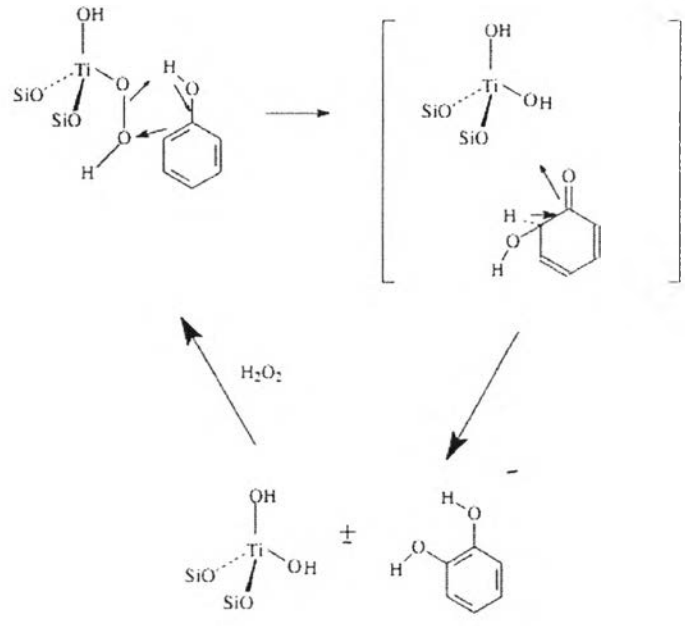

Figure 4.26 The mechanism of phenol hydroxylation to CAT via titanium [21].

HQ and CAT were further oxidized by H_2O_2 to BQ product. The formation of BQ is shown as Figure 4.27.

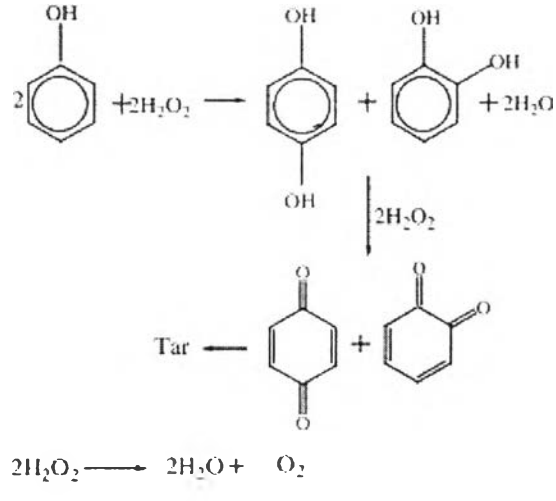

Figure 4.27 Schematic diagram of phenol hydroxylation with H_2O_2 and tar formation [25].

4.5 Conclusions

Iron-SBA-15, titanium-SBA-15, and bimetallic 0.01Fe-0.01Ti-SBA-15 were successfully synthesized via the sol gel process at room temperature using silatrane, ferric chloride, and titanium isopropoxide as silica, iron, and titanium sources, respectively, non-ionic surfactant Pluronic 123 as a structure-directing agent in highly acidic condition. SAXS and FE-SEM results showed that all samples still maintained 2D hexagonal mesoporous structure. N_2 adsorption-desorption results showed type (IV) isotherm with H1 hysteresis loop, exhibiting uniform pore as well as high surface area (631–763 m^2/g), large pore volume (0.621–0.971 cc/g), and pore size (3.93–5.21.nm). The results from DR-UV confirmed the metal incorporation with no extraframework. The highest phenol conversion at 37.96% with 100% selectivity of benzoquinone was obtained when using 1:1 molar ratio of phenol/H_2O_2 and 30 mg of 0.01Fe-0.01Ti-SBA-15 at 30 °C for 20 min. Metal leaching is not observed. However, the catalyst cannot be reused due to its instability.

4.6 Acknowledgments

This research work is supported by Ratchadapisake Sompote Endowment Fund, Thailand Research Fund, The Petroleum and Petrochemical College Chulalongkorn University, Thailand and The Center of Excellence on Petrochemical and Materials Technology, Thailand.

4.7 References

1. Norhasyimi R., A. Z. A. a. A. R. M., *American Journal of Applied Sciences.* 2010, 7(12), 1579-1586.
2. Bui, T. X.; Kang, S. Y.; Lee, S. H. and Choi, H., *J Hazard Mater.* 2011, 193, 156-63.
3. Huo, Q., Chapter 16 - Synthetic Chemistry of the Inorganic Ordered Porous Materials, in Modern Inorganic Synthetic Chemistry, X. Ruren, et al., Editors. 2011, Elsevier: Amsterdam. p. 339-373.

4. Samran, B.; White, T. and Wongkasemjit, S., *J. Porous Mater.* 2011, 18(2), 167-175.
5. Li, Y.; Feng, Z.; Lian, Y.; Sun, K.; Zhang, L.; Jia, G.; Yang, Q. and Li, C., *Microporous Mesoporous Mater.* 2005, 84(1–3), 41-49.
6. Zhang, Y.; Gao, F.; Wan, H.; Wu, C.; Kong, Y.; Wu, X.; Zhao, B.; Dong, L. and Chen, Y., *Microporous Mesoporous Mater.* 2008, 113(1–3), 393-401.
7. Jörg P. Thielemann, F. G., Robert Schlögl and Christian Hess, *the Beilstein Journal of Nanotechnology.* 2011, 2, 110–118.
8. Wu, Y.; Zhang, Y.; Cheng, J.; Li, Z.; Wang, H.; Sun, Q.; Han, B. and Kong, Y., *Microporous Mesoporous Mater.* 2012, 162(0), 51-59.
9. Wu, C.; Kong, Y.; Gao, F.; Wu, Y.; Lu, Y.; Wang, J. and Dong, L., *Microporous Mesoporous Mater.* 2008, 113(1–3), 163-170.
10. Sahu, D. R.; Hong, L. Y.; Wang, S.-C. and Huang, J.-L., *Microporous Mesoporous Mater.* 2009, 117(3), 640-649.
11. Zhang, H.; Tang, C.; Sun, C.; Qi, L.; Gao, F.; Dong, L. and Chen, Y., *Microporous Mesoporous Mater.* 2012, 151(0), 44-55.
12. Adam, F.; Andas, J. and Rahman, I. A., *Chem. Eng. J.* 2010, 165(2), 658-667.
13. Ivanchikova, I. D.; Lee, J. S.; Maksimchuk, N. V.; Shmakov, A. N.; Chesalov, Y. A.; Ayupov, A. B.; Hwang, Y. K.; Jun, C.-H.; Chang, J.-S. and Kholdeeva, O. A., *Eur. J. Inorg. Chem.* 2014, 2014(1), 132-139.
14. Adam, F.; Wong, J.-T. and Ng, E.-P., *Eur. J. Inorg. Chem.* 2013, 214(0), 63-67.
15. Samran, B.; Aungkutranont, S.; White, T. and Wongkasemjit, S., *Eur. J. Inorg. Chem.* 2011, 57(2), 221-228.
16. Johansson, E. M., Controlling the Pore Size and Morphology of Mesoporous Silica, in Nanostructured Materials Division Department of Physics, Chemistry and Biology (IFM). 2010, Linköping University: Sweden.
17. Ghazizadeh, M.; Badiei, A. and Sheikhshoaie, I., *Arabian J. Chem.* 2013.
18. Sun, J.; Meng, X.; Shi, Y.; Wang, R.; Feng, S.; Jiang, D.; Xu, R. and Xiao, F.-S., *J. Catal.* 2000, 193(2), 199-206.
19. Parida, K. M. and Mallick, S., *J. Mol. Catal. A: Chem.* 2008, 279(1), 104-111.

20. Yu, R.; Xiao, F.-S.; Wang, D.; Sun, J.; Liu, Y.; Pang, G.; Feng, S.; Qiu, S.; Xu, R. and Fang, C., *Catal. Today. 1999*, 51(1), 39-46.

21. Wróblewska, A., *Reaction Kinetics, Mechanisms and Catalysis*. 2013, 108(2), 491-505.

22. Dong, Y.; Niu, X.; Zhu, Y.; Yuan, F. and Fu, H., *Catal. Lett.* 2011, 141(2), 242-250.

23. Zhao, X.; Sun, Z.; Zhu, Z.; Li, A.; Li, G. and Wang, X., *Catal. Lett.* 2013, 143(7), 657-665.

24. Choi, J.-S.; Yoon, S.-S.; Jang, S.-H. and Ahn, W.-S., *Catal. Today*. 2006, 111(3–4), 280-287. *Microporous Mesoporous Mater*. 2008, 108(1–3), 56-64.

25. Liu, H.; Lu, G.; Guo, Y.; Guo, Y. and Wang, J., *Microporous Mesoporous Mater*. 2008, 108(1–3), 56-64.